Symbol Timing Synchronization for Uplink Multi-User Transmission in IEEE 802.11ax WLAN

Youngwook Son, *Student Member, IEEE,* Seongwon Kim, Seongho Byeon, *Member, IEEE,* and Sunghyun Choi. *Fellow, IEEE*
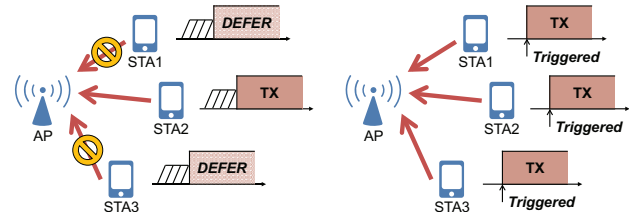
Abstract—Along with the proliferation of mobile devices and applications, IEEE 802.11 wireless local area network (WLAN) has become one of the most popular Internet access technologies. This leads to dense deployment of WLAN devices, and the calls for better user experience in such high-density WLAN environments are mounting. To keep pace with this increasing demand for high efficiency WLAN, IEEE 802.11ax, whose key advance is adopting uplink multi-user transmission (UL MU), is currently entering the final phase of standardization. The UL MU in 802.11ax WLAN, however, has a difficulty that stems from the intrinsically distributed nature of WLAN. Specifically, concurrent frames from multiple stations (STAs) are loosely synchronous in time, thus resulting in symbol timing misalignment which leads to poor decoding performance. In this work, we dissect the performance degradation caused by symbol timing misalignment and examine the required symbol timing conditions in receiving UL MU. Based on the analysis, we present a new two-step synchronization method to accommodate asynchronously arriving UL MU. We develop an 802.11ax link-level simulator and comparatively evaluate the proposed synchronization method via extensive simulations. Simulation results demonstrate that the proposed method successfully stabilizes UL MU data delivery even with large UL MU arrival timing deviations and the use of short cyclic prefix.

Index Terms—IEEE 802.11ax, high efficiency WLANs (HEW), symbol timing synchronization, OFDMA, multi-user MIMO

I. INTRODUCTION

In recent years, IEEE 802.11 wireless local area network (WLAN) has become an indispensable Internet access technology in our daily lives, along with the proliferation of mobile devices and applications. According to a research from industry, it is expected that there will be globally 541.6 million public WLAN hotspots by 2021, a six-fold increase from 94.0 million in 2016, and they will carry almost 50 percent of total IP traffic, reaching over 100 exabytes per month [1]. To keep pace with this increasing demand for mobile traffic and wireless connectivity, IEEE 802.11 standard is now preparing for another new deal as it has always been in its history.

IEEE 802.11n/ac, two representative amendments in the last decade, have achieved data rates up to 600 Mb/s and 6.9 Gb/s, respectively, by exploiting many state-of-the-art technologies in their physical layer (PHY) such as high-order modulation and coding scheme (MCS), channel bonding, and multiple input multiple output (MIMO) [2, 3]. After the completion of IEEE 802.11ac, consideration for user experience and high

Y. Son, S. Kim, and S. Choi are with the Department of ECE and INMC, Seoul National University, Seoul, Korea (email: {ywson, skim11}@mwnl.snu.ac.kr, schoi@snu.ac.kr).

S. Byeon is with Samsung Research, Samsung Electronics, Seoul, Korea (email: sh.byeon@samsung.com).

S. Choi and S. Kim are the corresponding authors of this paper.

(a) SU in conventional WLANs.   (b) UL MU in HE WLAN.

Fig. 1. Innovative change of IEEE 802.11ax realizes multiple transmitters at a time.

efficiency in dense deployment scenarios has boosted need for another evolutionary advance. Accordingly, a new task group was launched to develop the next amendment named IEEE 802.11ax, claiming for high efficiency (HE) WLAN. Most highlighted as a key driver in IEEE 802.11ax is the adoption of uplink multi-user transmission (UL MU), which allows multiple stations (STAs) to concurrently transmit to a common receiver, i.e., access point (AP). As illustrated in Fig. 1, it is absolutely a new paradigm contrary to single-user transmission (SU) in previous WLANs.

There are two enablers for UL MU: orthogonal frequency-division multiple access (OFDMA) and multi-user MIMO (MU-MIMO). Theoretically, both technologies allow interference-free concurrent transmissions in a perfectly synchronous network via frequency-division and spatial-division channel sharing among STAs. However, this is not the case usually in practical WLANs owing to the intrinsically distributed nature of 802.11 in that STAs are not tightly synchronized and are not strictly controlled as in cellular systems. In reality, multiple PLCP protocol data units (PPDUs)[1] transmitted in a UL MU can arrive at an AP with asynchronous timings. Although the timing misalignment only reduces to hundreds of nanoseconds thanks to tight hardware requirement of IEEE 802.11ax specification, we note that even such small misalignment could be fatal to the entire performance. Especially, since the conventional 802.11 receivers have not been originally designed for detecting asynchronous multiple signals, their synchronization modules are likely to be disrupted at the initial stage of frame reception in UL MU scenarios. Then the resulting timing errors cause inter-symbol interference (ISI) and inter-carrier interference (ICI), leading to severe aggravation of data decoding performance.

There have been several studies addressing the problem of

---

[1]PHY Layer Convergence Protocol (PLCP) is the upper sublayer of 802.11 PHY, and PPDU is a transmission unit of 802.11 PHY.

symbol timing synchronization and possible deleterious interference in asynchronous multi-user systems. [4–6] established the system model and timing requirements of asynchronous uplink OFDMA. They also provided comprehensive analysis and verification results for the interferences induced from synchronization errors among users, even though they focus only on OFDMA system with single spatial stream enabled. Meanwhile, it is identified in [7] that sufficiently long guard interval between adjacent symbols, namely cyclic prefix (CP) in OFDM, can be a buffer to accommodate the synchronization errors. Exploiting longer CP duration, however, sacrifices transmission efficiency leading to low network throughput. Other researches in [8, 9] present user-side approaches to resolve the asynchronous timings, that is, open-loop or closed-loop timing advance, which are not applicable at all to WLANs. Recent work in [10] illuminates UL MU-MIMO in asynchronous WLANs. It presents a new PHY design, as a substitute for the conventional minimum mean square error (MMSE) / zero-forcing (ZF) receivers, to decode the multiple misaligned streams. However, the extremely asynchronous scenarios assumed in this work are where STAs are not compliant with the timing requirement in 802.11ax standard specification. Thus it focuses on separating the concurrent streams using spatial filters, showing its feasibility for only up to four-stream MU-MIMO transmissions.

In this paper, we spotlight the two aspects of symbol timing synchronization problem for UL MU in IEEE 802.11ax WLAN specifically: 1) The impact of symbol timing errors on data decoding performance of OFDMA/MU-MIMO with the existence of asynchronous STAs and 2) malfunction of conventional 802.11 synchronization methods which fail to find proper symbol timing when receiving asynchronously superposed preambles. Based on the observations and analysis from those two aspects, we present a new symbol timing synchronization mechanism with enhanced functionality for capturing a desirable symbol timing, to accommodate asynchronously arriving PPDUs and mitigate ISI and ICI. Our contributions are summarized as follows.

- We first extend the previous analysis about symbol timing misalignment in OFDM systems to 802.11-specific UL MU scenarios including OFDMA/MU-MIMO transmissions. From this, we derive the theoretical symbol timing requirement for UL MU, which guarantees interference-free condition for all the participating STAs globally.
- Understanding the entire preamble processing flow at the conventional 802.11 receiver, we formulate the challenges in finding a proper timing for asynchronously arriving PPDUs, and then verify them by showing deterioration of the existing synchronization methods.
- We present a new two-step synchronization method, capable of finding a tolerable symbol timing within the range of practical requirement that is validated by simulation results. Both steps are originated considering specific 802.11ax PPDU format for UL MU, exploiting legacy preamble and extended HE preamble respectively.
- Extensive simulation-based performance evaluation shows that our proposed method reaches almost ideal performance

under given CP size. Specifically, while the primary time-domain synchronization step achieves higher precision in more asynchronous scenarios, subsequent fine calibration provides the consistent best performance facilitating the use of shorter CP.

To the best of our knowledge, this is the first work that identifies the symbol timing synchronization problem for standard-compliant UL MU in IEEE 802.11ax WLAN, and presents a solution to support the conventional MMSE/ZF receivers.

Note that all the analysis and evaluation throughout the paper have been carried by utilizing our elaborate 11ax link-level simulator, where all the features of IEEE 802.11ax PHY and lower medium access control (MAC) protocols are embedded by using IT++ libraries [11], at baseband signal processing level. Those features include new OFDM numerology of 802.11ax represented by symbol duration of 12.8 μs, new HE PPDU formats, and all sorts of transmission and reception (TX/RX) processing blocks for supporting OFDMA/MU-MIMO with MMSE receiver. For a UL MU implemented in our simulator, AP receives concurrent transmissions via OFDMA or OFDMA combined with MU-MIMO from up to 9 STAs, multiplexed within 20 MHz baseband, which is the smallest unit of operating bandwidth.

The rest of the paper is organized as follows. We introduce preliminary knowledge about symbol timing synchronization in terms of general MIMO-OFDM systems and IEEE 802.11 WLAN in Section II. In Section III, we elaborate UL MU specification and newly arising challenges for symbol timing synchronization. Our new synchronization mechanism for UL MU is presented in Section IV, and its performance is evaluated in Section V. Finally, Section VI concludes the paper.

II. PRELIMINARIES

A. Primer on OFDM Symbol Timing Synchronization

1) Case classification: We consider a $N \times N$ MIMO-OFDM system designed with discrete Fourier transform (DFT) size of N_{DFT} and cyclic prefix (CP) of N_{CP} samples prepended to every symbol. Let $X_m^{(i)}(k)$ represent the modulated constellation on the k-th subcarrier of the m-th symbol for the i-th spatial stream. Then the complex baseband samples of the symbol are constructed as

$$x_m^{(i)}(n) = \frac{1}{\sqrt{N_{\text{DFT}}}} \sum_{k=0}^{N_{\text{DFT}}-1} X_m^{(i)}(k)e^{j2\pi kn/N_{\text{DFT}}},$$
$$\text{for } -N_{\text{CP}} \leq n \leq N_{\text{DFT}} - 1, \quad (1)$$

and the consequent i-th TX stream is written as

$$x^{(i)}(n) = \sum_m x_m^{(i)}\big(n - m(N_{\text{DFT}} + N_{\text{CP}})\big). \quad (2)$$

The received baseband signal for the j-th RX chain can be written by

$$y^{(j)}(n) = \sum_i \left\{ h_{ji}(n) * x^{(i)}(n) \right\} + z^{(j)}(n)$$
$$= \sum_i \left\{ \sum_m \sum_{l=0}^{L-1} h_{ji}(l) \cdot x_m^{(i)}\big(n - l - m(N_{\text{DFT}} + N_{\text{CP}})\big) \right\}$$
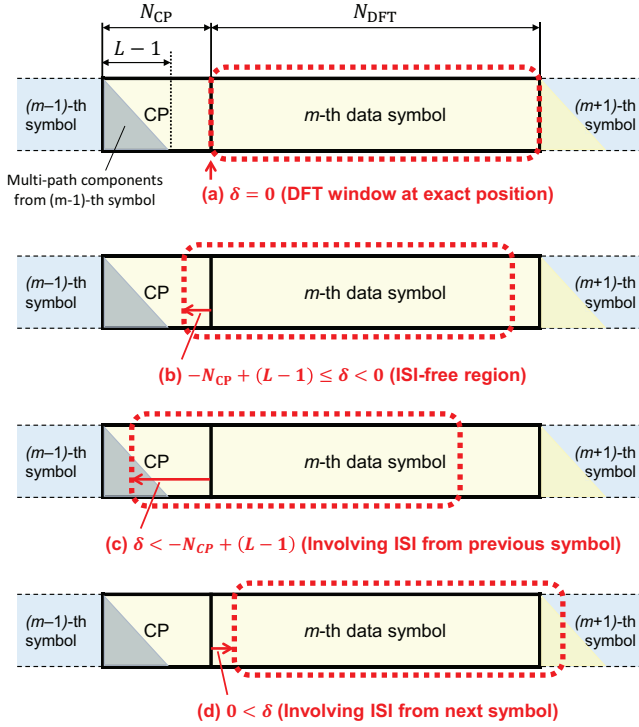$$+ z^{(j)}(n), \quad (3)$$

Fig. 2. Possible cases of receiver's DFT window position over an OFDM symbol: (a) Perfect synchronization, (b) ISI-free region, (c) involving ISI from the previous symbol, (d) involving ISI from the next symbol.

where $h_{ji}(n)$ is channel impulse response (CIR) between the i-th TX chain and the j-th RX chain, and $z^{(j)}(n)$ represents additive white Gaussian noise (AWGN). The total number of delay taps comprising the CIR, L, is supposed to be smaller than N_{CP} in a well designed OFDM system.

Four different cases of the receiver's DFT window over an OFDM symbol are illustrated in Fig. 2. We refer to the number of misaligned samples relative to the ideal symbol start as symbol timing offset (STO), δ, with the following relation:

$$\delta \triangleq \hat{n}_{\mathrm{DFT}} - n_{\mathrm{sym}}, \tag{4}$$

where n_{sym} denotes the sample index at which the transmitted OFDM symbol actually starts, and $\hat{n}_{\mathrm{DFT}}$ is its estimate at the receiver where the DFT window starts to be applied.

In Fig. 2, case (a) describes the perfect symbol timing synchronization, where receiver's DFT window is positioned at the exact range of the symbol so that δ equals zero. Assuming no frequency offset, the DFT output on the k-th subcarrier is represented as

$$Y_m^{(j)}(k) = \sum_i H_{ji}(k) X_m^{(i)}(k) + Z_m^{(j)}(k), \tag{5}$$

where $H_{ji}(k)$ denotes the channel gain of subcarrier k corresponding to the DFT of h_{ji}. We consider employing an MMSE receiver with the coefficient matrix $\mathbf{W}(\mathbf{k}) \in \mathbb{C}^{N \times N}$ given by

$$\mathbf{W}(\mathbf{k}) = \left\{ \mathbf{H}^{\mathrm{H}}(\mathbf{k})\mathbf{H}(\mathbf{k}) + N_0\mathbf{I} \right\}^{-1} \mathbf{H}^{\mathrm{H}}(\mathbf{k}), \tag{6}$$

where $\mathbf{H}(\mathbf{k}) \in \mathbb{C}^{N \times N}$ is the channel coefficient matrix ideally assumed with $\left\{ \mathbf{H}(\mathbf{k}) \right\}_{ji} = H_{ji}(k)$, and the superscript H of

a matrix denotes Hermitian transpose of the matrix. Then, the recovered symbol for the i-th stream can be achieved by

$$\tilde{X}_m^{(i)}(k) = \sum_j W_{ij}(k) Y_m^{(j)}(k)$$

$$= \left\{ \sum_j W_{ij}(k) H_{ji}(k) \right\} X_m^{(i)}(k) + \sum_{s \neq i} \left\{ I_{\mathrm{MMSE},i}^{(s)}(k) X_m^{(s)}(k) \right\}$$

$$+ \sum_j W_{ij}(k) Z_m^{(j)}(k), \tag{7}$$

where $W_{ij}(k) = \left\{ \mathbf{W}(\mathbf{k}) \right\}_{ij}$ and $I_{\mathrm{MMSE},i}^{(s)}(k) = \sum_j W_{ij}(k) H_{js}(k)$.

For case (b), DFT window starts somewhere within a specific range called *ISI-free region*. ISI-free region is the range which is not reached by delayed components of the previous symbol and is defined as

$$-N_{\mathrm{CP}} + (L-1) \leq \delta < 0. \tag{8}$$

In terms of the DFT output, cyclic shift property of the CP samples results in linear phase offsets across the subcarriers:

$$Y_m^{(j)}(k) = e^{j2\pi k\delta/N_{\mathrm{DFT}}} \sum_i H_{ji}(k) X_m^{(i)}(k) + Z_m^{(j)}(k). \tag{9}$$

As these phase offsets are not distinguished from the channel gains, the coefficient matrix $\mathbf{W}(\mathbf{k})$ naturally compensates them making no difference from (7).

Finally, cases (c) and (d) are the worst cases where DFT window starts outside the ISI-free region, that is, $\delta < -N_{\mathrm{CP}} + (L-1)$ or $0 < \delta$. In this case, the DFT input does not cover the desired m-th symbol entirely and rather contains irrelevant samples from an adjacent symbol. Then the consequent DFT output is corrupted by ISI in addition to symbol distortion from the collapsed orthogonality. Referring to [12], the resulting $Y_m^{(j)}(k)$ is given by

$$Y_m^{(j)}(k) = \alpha(\delta) e^{j2\pi k\delta/N_{\mathrm{DFT}}} \sum_i H_{ji}(k) X_m^{(i)}(k)$$

$$+ I_m^{(j)}(k, \delta) + Z_m^{(j)}(k), \tag{10}$$

where $\alpha(\delta)$ represents the attenuation factor due to the less number of useful samples and $I_m^{(j)}(k, \delta)$ is an additive interference term accounting for ISI and ICI, modeled as a zero-mean random variable with variance $\sigma_I^2(k, \delta)$. With the same MMSE receiver using ideal coefficient matrix $\mathbf{W}(\mathbf{k})$, the recovered symbol for the i-th stream can be obtained by

$$\tilde{X}_m^{(i)}(k) = \sum_j W_{ij}(k) Y_m^{(j)}(k)$$

$$= \alpha(\delta) e^{j2\pi k\delta/N_{\mathrm{DFT}}} \left\{ \sum_j W_{ij}(k) H_{ji}(k) \right\} X_m^{(i)}(k)$$

$$+ \alpha(\delta) e^{j2\pi k\delta/N_{\mathrm{DFT}}} \sum_{s \neq i} \left\{ I_{\mathrm{MMSE},i}^{(s)}(k) X_m^{(s)}(k) \right\}$$

$$+ \sum_j W_{ij}(k) \left\{ I_m^{(j)}(k, \delta) + Z_m^{(j)}(k) \right\}. \tag{11}$$

2) SINR degradation: As a consequence of the analysis above, average signal-to-interference-plus-noise-ratio (SINR) for the i-th spatial stream on subcarrier k is given depending on δ as[2]

[2]Note that (12) indicates the upper limit of average SINR degraded under the impact of STO, since it has been derived assuming the ideal channel coefficients. In practice, STOs and thermal noises could further induce channel imperfection at the receiver, thus spoiling the decoding process.
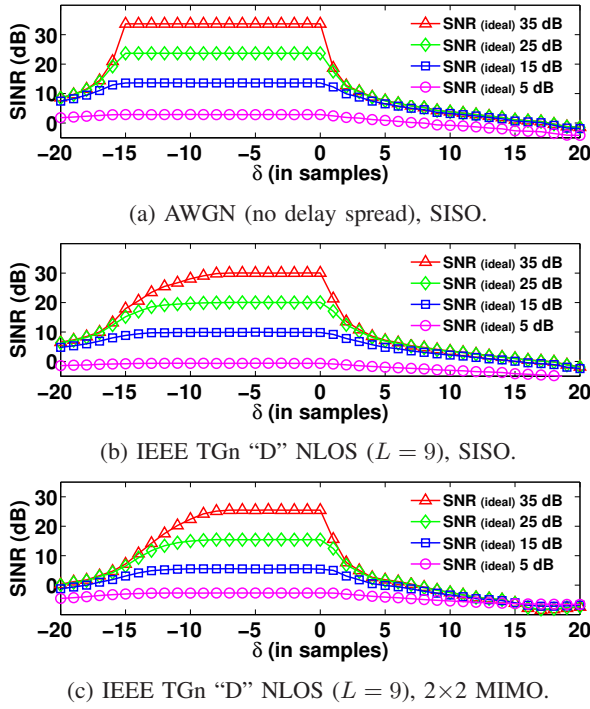
(a) AWGN (no delay spread), SISO.

(b) IEEE TGn "D" NLOS ($L = 9$), SISO.

(c) IEEE TGn "D" NLOS ($L = 9$), 2×2 MIMO.

Fig. 3. Effective SINR versus STOs (δ) under various ideal SNR levels, estimated by EVM [13] in a general SISO/MIMO-OFDM system with $N_{\mathrm{DFT}} = 64$ and $N_{\mathrm{CP}} = 16$.

$$\mathrm{SINR}_k^{(i)}(\delta) =$$
$$\frac{\alpha^2(\delta)\left|\sum_j W_{ij}(k)H_{ji}(k)\right|^2 P_T^{(i)}}{\alpha^2(\delta)\sum_{s \neq i}\left|I_{\mathrm{MMSE},i}^{(s)}(k)\right|^2 P_T^{(s)} + \left\{\sigma_I^2(k,\delta) + N_0\right\}\sum_j\left|W_{ij}(k)\right|^2}, \tag{12}$$

where $P_T^{(i)}$ is the average power of the i-th TX stream, on which additive interference power, $\sigma_I^2(k,\delta)$, also depends. For $-N_{\mathrm{CP}} + (L-1) \leq \delta \leq 0$, power attenuation $\alpha^2(\delta)$ and additive interference $\sigma_I^2(k,\delta)$ attributed to the symbol timing offset reduce to unity and zero, respectively.

To quantitatively figure out the impact of δ on SINR performance, we calculate error vector magnitude (EVM) in the I-Q plane between the ideal TX symbol and the recovered symbol at the MMSE receiver, for different δ values. Referring that the effective SINR can be approximated as the reciprocal of the squared EVM [13], Fig. 3 plots the effective SINR versus δ under some ideal SNR levels ($P_T^{(i)}/N_0$), i.e., SNR achieved with perfect synchronization. $N_{\mathrm{DFT}} = 64$ and $N_{\mathrm{CP}} = 16$ are assumed, and we have applied random CIR instances from AWGN ($L = 1$) and IEEE TGn "D" NLOS channel [14], which models typical indoor office environment ($L = 9$).

The result verifies the case classification of symbol timing offset illustrated in Fig. 2 and the existence of the ISI-free region by observing that SINR is maintained almost the same for $-N_{\mathrm{CP}} + (L-1) \leq \delta \leq 0$ and rapidly decreases outside the region. Since the additive interference power, $\sigma_I^2(k,\delta)$, becomes dominant at farther δ's from the ISI-free region, SINR curves converge regardless of the ideal SNR level. For fading channels with $L > 1$, meanwhile, small negative STOs outside the ISI-free region but within CP, i.e., $-N_{\mathrm{CP}} \leq \delta <$
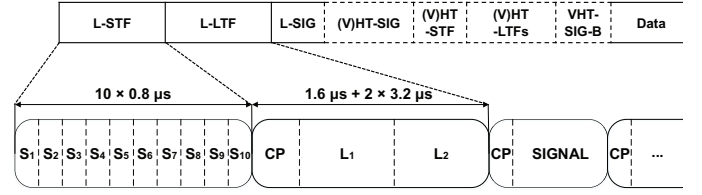

Fig. 4. IEEE 802.11 legacy PLCP preamble structure.

$-N_{\mathrm{CP}} + (L-1)$ yield less drastic SINR degradation compared to $\delta > 0$. This difference between positive and negative values of δ is attributed to the diminishing power delay profile (PDP) of CIR, which makes ISI from the previous symbol less influential than that from the next symbol.

B. Symbol Timing Synchronization for IEEE 802.11 WLAN

In IEEE 802.11 WLANs, legacy PLCP preamble is always at the head of every PPDU and utilized by receiver to acquire the symbol timing for aligning its DFT window with the following OFDM data symbols. In this section, we first provide a brief description for the preamble structure of IEEE 802.11 PPDU, and then introduce various 802.11-specific symbol timing synchronization techniques in literature.

PLCP preamble structure: Fig. 4 shows the legacy PLCP preamble that is prepended to all the practical IEEE 802.11 PPDU formats, namely, regardless of the standard amendment version, e.g., 11a/b/g (Legacy) and 11n mixed-format (HT-MF) and 11ac (VHT). This uniformity helps maintain compatibility among heterogeneous standard-compliant WLAN devices.

Specifically, the preamble is divided into two portions. The first is legacy short training field (L-STF), which consists of ten repetitions of a $0.8~\mu s$ short training symbol. This field, by virtue of its repetitive nature and good correlation properties, is utilized for frame detection, automatic gain control (AGC), symbol timing synchronization, and coarse frequency offset estimation. The other portion is legacy long training field (L-LTF), which contains two repetitions of a $3.2~\mu s$ long training symbol with a $1.6~\mu s$ CP. The main purposes of L-LTF are symbol timing synchronization, fine frequency offset estimation, and channel estimation.

Correlation metrics: Now we introduce two correlation metrics typically used by 802.11 receivers for processing the preamble fields:

$$a(n) = \frac{\left|\sum_{i=0}^{K_a-1} r(n-i) \cdot r(n-i-d)^*\right|}{\sqrt{\sum_{i=0}^{K_a-1}|r(n-i)|^2}\sqrt{\sum_{i=0}^{K_a-1}|r(n-i-d)|^2}}, \tag{13}$$

$$c(n) = \frac{\left|\sum_{i=0}^{K_c-1} r(n-K_c+1+i) \cdot s(i)^*\right|}{\sqrt{\sum_{i=0}^{K_c-1}|r(n-K_c+1+i)|^2}\sqrt{\sum_{i=0}^{K_c-1}|s(i)|^2}}, \tag{14}$$

where $r(n)$ is the received time-domain sample, $s(n)$ is the known sequence stored at the receiver, and K_a and K_c denote the window size parameters. Basically, these two metrics are known to be first introduced by Schmidl and Cox in [15].

Eq. (13) represents the normalized auto-correlation calculated using the incoming signal and its one-symbol delayed version over the sliding window of length K_a. The metric is usually applied to L-STF with the delay $d = 16$ (mapped to 0.8 μs with 20 MHz sampling rate). Its value exceeding a certain threshold indicates an incoming 802.11 PPDU detected, after which the receiver tries to search a sample index corresponding to the start of L-LTF by observing when the auto-correlation reaches and stays at the peak level.

Meanwhile, (14) calculates the cross-correlation between the incoming signal and the known training sequence, and K_c is determined depending on which training sequence among L-STF and L-LTF is chosen as $s(n)$. For example, when exploiting L-LTF samples, K_c is usually set to the number of samples in a long training symbol (64 with 20 MHz sampling rate) and as a result of calculation two separated peaks appear at the end instants of long training symbols, L_1 and L_2 in Fig. 4.

Symbol timing synchronization techniques: Most symbol timing synchronization techniques for 802.11 system in literature utilize either of those two correlation metrics or both in combination.

As for the conventional SISO-OFDM systems before 802.11n, [16] proposed a cross-correlation based method applicable to L-LTF. Two separate peaks are obtained for long training symbols, and the method detects the first peak exceeding a certain threshold which indicates transition between L-STF and L-LTF. Fort's method [17] is based on a modified auto-correlation function utilizing accumulators, which allows a clear peak instead of a plateau. [18] proposed a mechanism which jointly utilizes auto-correlation and cross-correlation of L-STF for symbol boundary detection, unaffected by the arbitrary timing when PPDU detection and AGC settlement are completed. Another algorithm proposed in [19] adopted a two-step approach, where the auto-correlation using L-STF gives a coarse symbol timing and then fine timing synchronization is accomplished by detecting the first cross-correlation peak of L-LTF. To deal with the plateau problem, i.e., the difficulty of auto-correlation based symbol timing synchronization methods due to the auto-correlation plateau rather than a single peak, a differentiator is concatenated providing sharper peaks in the coarse step. Other than correlation based methods, there have been some maximum-likelihood (ML) based algorithms in literature [20]. They are considered impractical, however, due to excessive computational overhead as well as not providing comparable accuracy to correlation based methods, as verified by [21].

With the advent of MIMO-OFDM WLANs since 802.11n, the use of cyclic shift diversity (CSD) which induces multiple cross-correlation peaks, i.e., *pseudo multi-paths*, has been the top priority concern for the symbol timing synchronization problem. To address the pseudo multi-path problem, [22] proposed utilizing an SIR-based metric for fine synchronization, which is calculated as the weighted sum of the cross-correlation of L-LTF. The method also resolves arbitrary AGC settlement timing and the plateau problem by adopting auto-correlation based coarse step with a sliding window differen-

tiator, similar to that in [19]. On the other hand, [23] proposed an advanced version of Chang's method [18], covering the pseudo multi-path problem by adopting SNR-varying threshold for the boundary detection. Finally, the proposed method in [24] introduces conjugate symmetric correlator using L-LTF for fine synchronization, instead of conventional cross-correlation based manner. While this algorithm guarantees moderate performance even with CSD-applied preambles, it has a drawback in the timeliness of channel estimation since the whole L-LTF samples are needed to calculate the conjugate symmetric correlation.

III. Symbol Timing Synchronization for 802.11ax Uplink Multi-User Transmission

In the upcoming HE WLAN standard 802.11ax, most highlighted as a key driver is UL MU, which allows multiple STAs to transmit concurrently to a common AP via OFDMA, MU-MIMO, or a mixture of the both technologies. In this section, we present the specification of 802.11ax UL MU, and then elaborate on the emerging challenges regarding symbol timing synchronization for UL MU.

A. Standard Specification of UL MU

IEEE 802.11ax standard specifies that UL MU procedure is necessarily initiated by the AP announcing a *Trigger frame*, as shown in the upper part of Fig. 5. Participating STAs are then solicited for UL MU in HE trigger-based (TB) PPDU format, short inter-frame spacing (SIFS) after receiving the Trigger frame. Basically, this trigger-driven procedure is for delivering the instruction about the following UL MU such as resource unit (RU) allocation, PPDU duration, MCS to be used, CP length, and so on, but also aims at synchronizing the start instant of the transmissions from distributed STAs, by means of the reference signaling prior to UL MU. Unfortunately, this way of UL MU coordination via Trigger frame, however, does not ensure that all the transmitted signals arrive at the AP at the exactly same time, which could severely disrupt the receiving performance as will be detailed later.

HE TB PPDU, as a newly defined frame format for UL MU in 802.11ax, is largely divided into two distinct parts— *Common* fields with legacy OFDM structure and *user-specific* fields with the new numerology of 802.11ax. Common fields consist of the legacy preamble fields described in Section II-B and several PHY header fields. They populate the whole bandwidth of the transmission channel like the legacy 802.11 frame formats, regardless of the allocated OFDMA RU. The only difference from the legacy 802.11 frames is that those PHY headers are generated with the information bits indicated by the Trigger frame, which are common for all the participants of UL MU. This means that the concurrent frames in a UL MU all have the identical waveforms for the common fields, so the preamble and PHY header fields are superposed at the AP after going through independent fading channels.

Subsequent user-specific fields are where OFDMA or MU-MIMO PHY is actually applied to support data delivery via UL MU. Unlike the legacy 802.11 frames, the user-specific fields only populate the OFDMA RU allocated for that UL
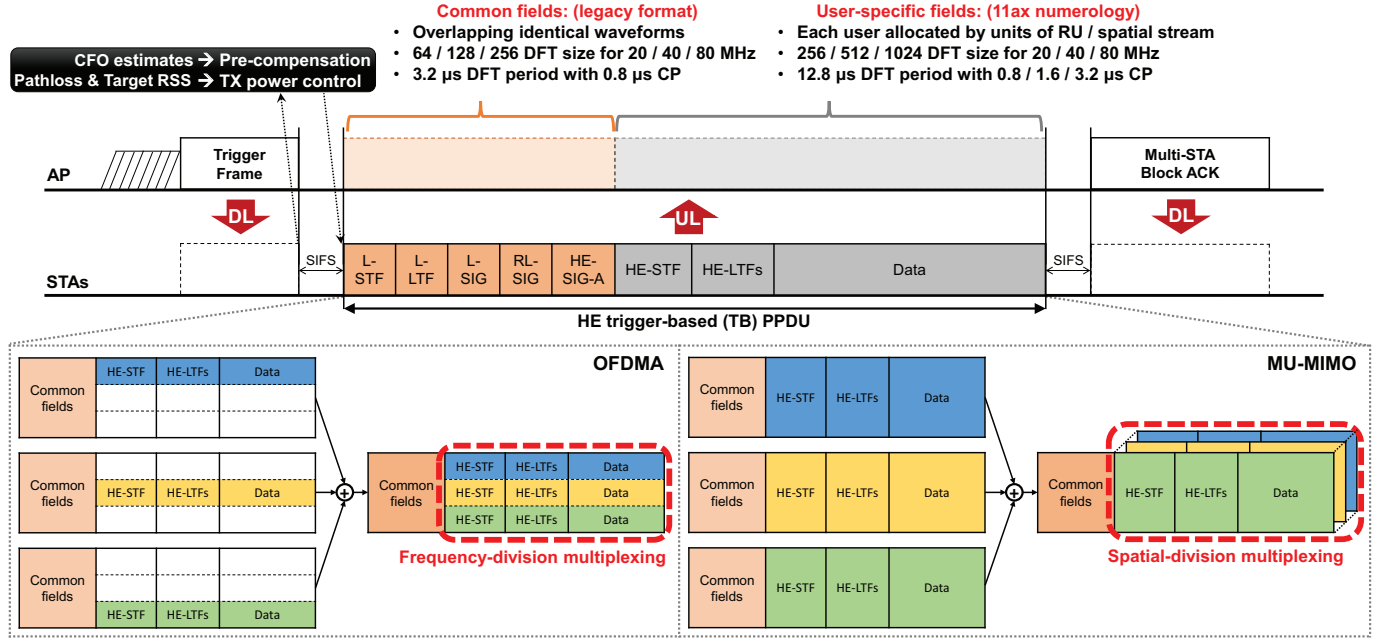
Fig. 5. Description of the entire UL MU procedure and HE trigger-based (TB) PPDU structure for OFDMA / MU-MIMO.

MU within the whole bandwidth of the transmission channel, conveying user-specific preamble fields and data symbols. The HE preamble fields contain HE-LTFs to provide means for the receiver to retrain the channel gains, which are essential to decode the following data symbols. Note that for the remainder of the paper we refer to those frames with the HE TB PPDU format, which are transmitted in response to Trigger frame, as "UL MU frames" or "concurrent frames" to avoid confusion.

B. Problem Description

The preceding Trigger frame coordinates UL MU such that participating STAs start their transmission simultaneously SIFS after receiving the Trigger frame. In terms of microscopic timing, however, it is not guaranteed that all those concurrent frames reach the AP at the exactly same time, since each STA has own round-trip delay (RTD) and local oscillator (LO) clock which makes its perceived SIFS interval. Concretely, the timing requirement in 802.11ax specifies that a STA who participates in UL MU shall ensure the arrival time of its transmitted frame at AP to be within $\pm 0.4 \ \mu s$ of SIFS + RTD from the end of Trigger frame transmission. It also notes that STAs are not expected to measure or compensate for their RTDs [25]. Hence, for standard-compliant devices, concurrent UL MU frames can arrive at the AP with timing deviation of up to $0.8 \ \mu s$ + maximum RTD according to the environment.

Having distinct symbol start index n_{sym}^u for the UL MU frame originated from u-th STA, we define θ_u as the deviation of arrival timing with respect to the earliest arriving frame in UL MU:

$$\theta_u \triangleq n_{\text{sym}}^u - \min_{v \in U} \left\{ n_{\text{sym}}^v \right\}, \qquad (15)$$

where U is a whole set of STAs who participate in the UL MU. Then the received baseband signal covering UL MU can

be rewritten as

$$y^{(j)}(n) = \sum_{u \in U} \left\{ h_j^u(n) * x^u(n - \theta_u) \right\} + z^{(j)}(n)$$
$$= \sum_{u \in U} \left\{ \sum_{l=0}^{L_u - 1} h_j^u(l) \cdot x^u(n - \theta_u - l) \right\} + z^{(j)}(n) \qquad (16)$$

where $x^u(n)$ and $h_j^u(n)$ denote the transmitted signal from u-th STA and its CIR with L_u taps to the j-th RX chain at the AP, respectively, and l is the tap index.

Fig. 6 illustrates the situation where concurrent UL MU frames reach the AP at slightly different timings from each other. Now we provide an investigation into the effect of asynchronous frame arrivals at AP's UL MU receiver, which is twofold: on processing the legacy preamble fields and on decoding the following data symbols.

1) Processing legacy preamble fields: Focusing on the legacy preamble fields, we can see that the incoming training symbols are superposed asynchronously according to their arrival timings, thus making it much harder to find a proper symbol timing.

To be specific, as the detected signal strength fluctuates with each arriving frame, the AGC settlement gets delayed compared to when there is a single transmitter. This makes only a few intact L-STF samples available for the synchronization purpose. In addition, the auto-correlation plateau tends to fall gradually around the boundary between L-STF and L-LTF, since the L-STF from the late arriving frames maintains their repetitive pattern of $0.8 \ \mu s$ period even after the early arriving frames have moved on to L-LTF. As a result, accuracy of the auto-correlation based boundary detection methods is highly aggravated, even when combined with a differentiator as in [19, 22].
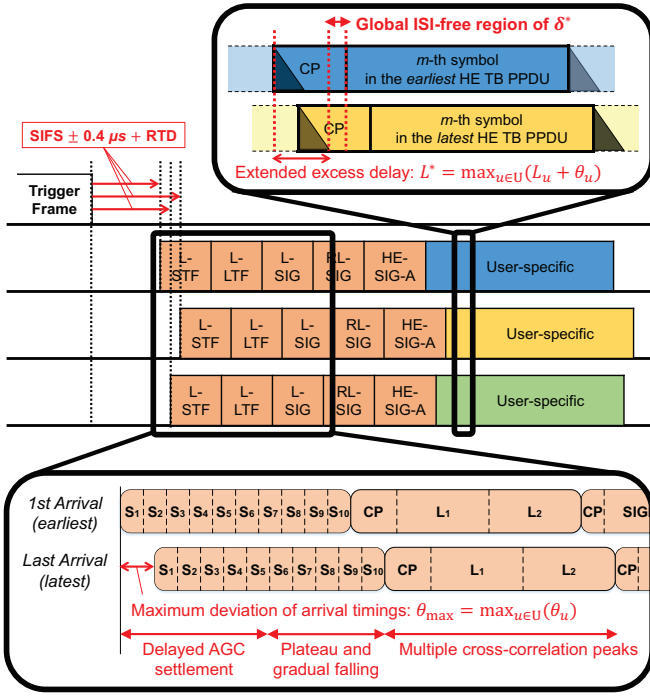
Fig. 6. Effects of asynchronous arrival timings among UL MU frames: 1) Global ISI-free region for DFT window, and 2) difficulty in processing legacy preamble fields.
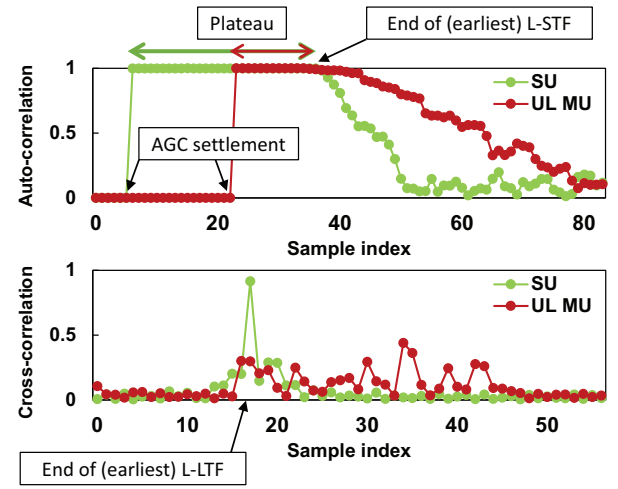

Fig. 7. Comparison of the conventional correlation metrics between SU and 9-user UL MU: Auto-correlation in (13) with $K_a = 16$ & $d = 16$ for L-STF, and cross-correlation in (14) with $K_c = 64$ for L-LTF (time samples in 20 MHz sampling rate).

Meanwhile, the cross-correlation in (14) generates multiple peaks, every time its stored training sequence matches to an identical one from each UL MU frame, which is similar to the pseudo multi-path problem in MIMO transmissions. While the CSDs applied to the legacy preamble fields have pre-defined negative values up to -0.2 μs, thus prone to STOs within the ISI-free region, the multiple peaks generated by asynchronously incoming training symbols tend to be put behind the earliest peak, obviously outside of the ISI-free region. Fig. 7 illustrates an example of auto-correlation and cross-correlation applied to the asynchronously superposed preambles, distinct from SU case.

Above all, most challenging about processing the superposed preambles is the randomness in that those phenomena incurred in correlation metrics are wholly unpredictable, depending on the case-by-case distribution of arrival timings, θ_u's and its maximum deviation, $\theta_{\max} = \max_{u \in U}(\theta_u)$. Consequently, existing correlation-based methods can be severely disrupted when employed for receiving UL MU at the AP, as will be verified in Section V.

It is notable that, in practice, most commercial off-the-shelf (COTS) devices have the second capture capability [26] in receiving PLCP preamble, which is the capability to resynchronize to a newly incoming stronger signal than currently being received one. Hence, COTS devices are likely to synchronize to the strongest signal regardless of the arrival order. This "strongest first" behavior, however, is not desirable for receiving concurrent frames in UL MU scenario, considering practically imperfect power pre-correction and time-varying characteristics of the wireless channel. Moreover, different from cellular communication systems that resolve the sim-

ilar synchronization problem by supporting timing advance operation at the transmitter side, 802.11 WLAN does not provide any functionality to pre-compensate the arrival timing deviation of concurrent transmissions.

2) Decoding data symbols: Looking into the data symbols, on the other hand, receiver's DFT window should satisfy ISI-free for all the scattered UL MU frames to avoid mutual ISI and ICI among STAs. Accordingly, ISI-free region shrinks compared to the SU case in Section II-A, thus making symbol timing synchronization for UL MU still more challenging. Now we should consider the global ISI-free region, that is, the intersection of all the ISI-free regions for concurrent UL MU frames. Equivalently, we can regard the received signal in (16) as SU that is being affected by a virtual CIR with an extended tap length of $L^* = \max_{u \in U} \{L_u + \theta_u\}$, referring to [5]. With the maximum deviation in the worst scenario, 1.3 μs, including 0.5 μs RTD difference and IEEE TGn "D" NLOS channel, for instance, $L^* = 26 + 9 = 35$, being larger than the medium CP length, i.e., 32 samples.

As illustrated in Fig. 6, the global ISI-free region, if it exists, then can be given as

$$-N_{\mathrm{CP}} + (L^* - 1) \le \delta^* \le 0, \tag{17}$$

where δ^* denotes STO with respect to the earliest UL MU frame, given by

$$\delta^* \triangleq \hat{n}_{\mathrm{DFT}} - \min_{u \in U} \{n_{\mathrm{sym}}^u\}. \tag{18}$$

Note that for $L^* - 1 > N_{\mathrm{CP}}$, there exists no global ISI-free region that guarantees zero mutual interference among STAs.

When satisfying the global ISI-free region, the DFT output on the k-th subcarrier is rewritten as

$$Y_m^{(j)}(k) = \sum_{u \in U_k} \left\{ e^{j2\pi k \delta_u / N_{\mathrm{DFT}}} H_j^u(k) X_m^u(k) \right\} + Z_m^{(j)}(k),$$

$$\text{where } \delta_u = \delta^* - \theta_u = \hat{n}_{\mathrm{DFT}} - n_{\mathrm{sym}}^u, \tag{19}$$

while U_k represents a set of STAs, who are assigned the RU containing the k-th subcarrier, i.e., $U_k \triangleq \{u \mid u \in U \text{ and } X_m^u(k) \neq 0 \text{ for } \forall m \text{ in user-specific fields}\}$. In this case, (19) just involves the linear phase offsets as in (9), yielding no SINR degradation.

On the other hand, if the AP's DFT window starts somewhere outside the global ISI-free region or the global ISI-free region does not exist, the output suffers from self or mutual interference between STAs as well as signal distortion, according to respective δ_u's:

$$Y_m^{(j)}(k) = \sum_{u \in U_k} \left\{ \alpha(\delta_u) e^{j2\pi k \delta_u / N_{\text{DFT}}} H_j^u(k) X_m^u(k) \right\}$$
$$+ \sum_{u \in U} I_{u,m}^{(j)}(k, \delta_u) + Z_m^{(j)}(k), \qquad (20)$$

where $\alpha(\delta_u)$ and $I_{u,m}^{(j)}(k, \delta_u)$ reduce to unity and zero, respectively, for δ_u satisfying each local ISI-free region, $-N_{\text{CP}} + L_u - 1 \leq \delta_u \leq 0$.

Similar to (12), average SINR for the u-th frame in UL MU is thus obtained by

$$\text{SINR}_k^u(\{\delta_v | v \in U\}) = \frac{\alpha^2(\delta_u) \big| \sum_j W_{uj}(k) H_j^u(k) \big|^2 P_T^u}{\sigma_{\text{MMSE}}^2 + \{\sigma_{I,\text{tot}}^2 + N_0\} \sum_j |W_{uj}(k)|^2},$$

where $\sigma_{\text{MMSE}}^2 = \sum_{v \in U_k, v \neq u} \left\{ \alpha^2(\delta_v) \big| \sum_j W_{uj}(k) H_j^v(k) \big|^2 P_T^v \right\},$

$\sigma_{I,\text{tot}}^2 = \sum_{v \in U} \sigma_I^2(k, \delta_v), \qquad (21)$

when AP adopts an MMSE receiver with the ideal coefficient matrix $\mathbf{W}(k)$ generated from $\mathbf{H}(k)$ whose elements are $\{\mathbf{H}(k)\}_{ju} = H_j^u(k)$. Although (16)–(21) above have been derived for single-stream transmission per STA in UL MU, straightforwardly they can be extended to STAs each transmitting multiple streams, combined with OFDMA, MU-MIMO or a mixture of both.

IV. PROPOSED SYMBOL TIMING SYNCHRONIZATION

As described in the previous section, symbol timing synchronization for 802.11ax UL MU involves the distinct challenges from SU case, that is, conventional correlation metrics are disrupted by superposed preambles, and the ISI-free region for DFT window position shrinks. In this section, we first examine how precise the symbol timings should be to ensure "good" performance in terms of data delivery via UL MU, and then propose a new symbol timing synchronization mechanism for AP's UL MU receiver. Our solution addresses asynchronous frame arrivals in order to accommodate UL MU into the backward-compatible 802.11 WLAN, by exploiting two key breakthroughs: Remaining repetitive nature on superposed training symbols and per-STA channel estimates demultiplexed in frequency domain.

A. Performance Requirement

To investigate the desirable performance of new symbol timing synchronization for 802.11ax UL MU, we have tested on our 802.11ax link-level simulator how badly degraded the

TABLE 1: Simulation settings.

| Model & parameter	Value
Bandwidth	20 MHz
Channel model	TGn "D" NLOS
Number of STAs in UL MU	9 (OFDMA alone) / 8 (with MU-MIMO)
Number of antennas	Each STA: 1, AP: 1 (OFDMA alone)
	Each STA: 1, AP: 4 (with MU-MIMO)
Maximum arrival deviation ($\theta_{\max}$)	16 (0.8 μs) / 26 (1.3 μs)
Frequency & power difference	Ideal pre-correction assumed
SNR	@~90% MUDR with $\theta_u = 0$ for all STAs
	and perfectly synchronized to $\delta^* = 0$
RU allocation	26-tone $\times$ 9 (OFDMA alone)
	106-tone $\times$ 2 (with MU-MIMO)
Number of spatial streams per RU	1 (OFDMA alone) / 4 (with MU-MIMO)
Cyclic prefix	1.6 μs (medium size)
Modulation & coding scheme	MCS3 (16-QAM, R=1/2)
	MCS7 (64-QAM, R=5/6)
MPDU size	1,500 bytes (no aggregation)
CSD	Following standard specification
Foward error correction (FEC)	Binary convolutional code (BCC)
	and soft-decision Viterbi decoder at receiver
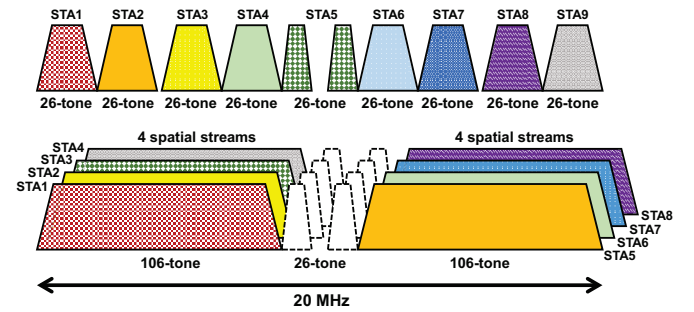
Fig. 8. Two exemplary UL MU scenarios within 20 MHz: OFDMA alone with 9 participants assigned (upper) and OFDMA+MU-MIMO with 8 participants assigned (lower).

data delivery of UL MU is under different δ^*'s and different values of an environmental parameter, namely, maximum deviation of arrival timings, $\theta_{\max}$.

For each simulation run, UL MU frames arrive at the AP having independent random arrival timings following the uniform distribution with $\theta_{\max} = 16$ (0.8 μs) and 26 (1.3 μs). These two values are chosen representatively as they each correspond to the maximum tolerance without RTD difference specified in the standard and the maximum deviation in the worst scenario having RTD difference up to 0.5 μs. Using the channel traces from TGn "D" NLOS model with $L = 9$, the global ISI-free region for each value of $\theta_{\max}$ is given as $-N_{\text{CP}} + 25 \leq \delta^* \leq 0$ and $-N_{\text{CP}} + 35 \leq \delta^* \leq 0$, respectively, according to (17). Thus, with 1.6 μs CP ($N_{\text{CP}} = 32$), for example, the global ISI-free region for $\theta_{\max} = 16$ is $-7 \leq \delta^* \leq 0$, whereas no global ISI-free region exists for $\theta_{\max} = 26$. We assume the ideal frequency and power pre-correction at STAs, so that there exists no frequency offset and no difference in the average signal strength among the received concurrent frames. Instead of the packet delivery ratio (PDR) commonly used in SU, we newly define MU data delivery ratio (MUDR) as the ratio of the number of successfully received MPDUs to the number of total MPDUs transmitted in a UL MU, in order to represent a metric to approximate "PDR per UL MU." As in discussing PDR for conventional SU, we set MUDR around ~90% as the desirable performance of interest, which is considered an allowable reference level under given
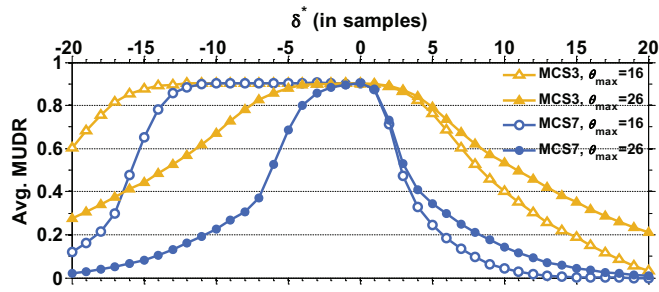
(a) OFDMA alone scenario, where 9×26-tone RUs within 20 MHz deliver single-stream data fields originated from 9 STAs.
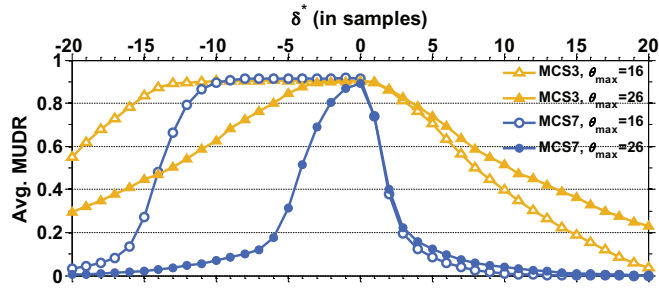
(b) OFDMA+MU-MIMO scenario, where 2×106-tone RUs within 20 MHz each deliver four spatial streams of data fields originated from 8 distinct STAs.

Fig. 9. UL MU data delivery ratio versus δ^* for different MCSs and maximum deviation of arrival timings, $\theta_{\max}$.

SNR in WLAN environments.[3] All the simulation settings are summarized in Table 1.

We set up two different UL MU scenarios for simulation, as illustrated in Fig. 8: 1) OFDMA alone where 9 concurrent frames are transmitted each populating one of the 9 26-tone RUs within 20 MHz for its user-specific fields, and 2) OFDMA combined with MU-MIMO where 8 concurrent frames are transmitted each populating one of the two 106-tone RUs within 20 MHz for its user-specific fields, forming four spatial streams per RU.

Fig. 9 shows average MUDR versus δ^* for the two scenarios, with SNR set to some fixed levels at which perfectly synchronous UL MU (zeros for all θ_u's and δ_u's) achieves about 90% MUDR. The overall trend of MUDR degradation seems similar to SINR degradation in Fig. 3, especially when $\theta_{\max}$ is 16, since δ^*'s within the global ISI-free region guarantees no SINR degradation for the whole UL MU frames. The only difference is that we need to search the desirable symbol timing within tighter range than in receiving SU, as the global ISI-free region shrinks under large deviation of frame arrival timings.

Interestingly, for $\theta_{\max} = 26$ where the global ISI-free region does not exist, capturing the symbol timing of the earliest UL MU frame, namely, δ^* near to zero still works better than under other possible symbol timings, yielding about 90% average MUDR comparable with the perfectly

synchronous UL MU. This resilience, however, requires even tighter synchronization performance, depending on MCS and the number of spatial streams used for UL MU. For instance, just a single sample offset ($50\ ns$) from the exact symbol timing of the earliest UL MU frame noticeably aggravates the average MUDR for the second scenario using MCS7 under $\theta_{\max} = 26$, as shown in Fig. 9(b).

From the observation above, we can conclude that on the average sense "symbol timing of the earliest one among all the concurrent UL MU frames" should be a reference target point for the synchronization of UL MU, considering all the practical UL MU scenarios and surrounding environments. Moreover, this target symbol timing should be tightly attained, compared to conventional SU scenarios having a sufficient buffer region within CP. Finally, comparing the two UL MU scenarios, it is also evident that MU-MIMO requires tighter synchronization than OFDMA alone, as demultiplexing spatial streams is highly sensitive to the accuracy of channel matrix, additive interference, and distortion caused by STO.

B. Proposed Method

Now, we propose a new symbol timing synchronization mechanism for AP's UL MU receiver, which targets finding the symbol timing of the earliest frame in a UL MU. As elaborated in Section III, it is infeasible to get a perfect metric in a conventional form which exploits legacy preamble fields, covering all the UL MU cases with arbitrary arrival timing distributions. For this reason, we instead focus on capturing somewhere within or adjacent to the global ISI-free region and then finding the specific STO of each UL MU frame, δ_u, in frequency domain. To this end, it is necessary to utilize demultiplexed per-STA channel gains obtained from HE-LTFs, rather than legacy preamble fields bearing indivisibly mixed channel response over the whole bandwidth.

1) Time-domain synchronization: We perform autocorrelation on the legacy preamble fields with distinct window size and sample delay from other conventional methods. Concretely, it calculates (13) with $K_a = 64$ and $d = 64$ for 20 MHz sampling rate in order to detect $\hat{n}_{\mathrm{LSIG}}$, i.e., the estimated boundary between L-LTF and L-SIG, by

$$\hat{n}_{\mathrm{LSIG}} = \arg\max_n \{a(n)|_{K_a=64, d=64}\}. \qquad (22)$$

Unlike any other previous methods exploiting only L-STF for the auto-correlation based metric, we adopt parameter values for detecting L-LTF, motivated by the fact that repetitive pattern of 3.2 μs period survives on the intersection of overlapping L-LTFs as depicted in Fig. 10. The repetition lasts at least longer than the whole 3.2 μs duration of a long training symbol, assuming that the maximum arrival deviation $\theta_{\max}$ at AP is under 1.3 μs.

The proposed auto-correlation metric is not affected by the unknown timing of AGC settlement, which is especially delayed in receiving UL MU, leading to lack of available L-STF samples. Moreover, exploiting L-LTF for the symbol timing synchronization purpose in UL MU does not incur any drawback in terms of channel estimation latency, since the receiver AP has no need to read the PHY headers of UL
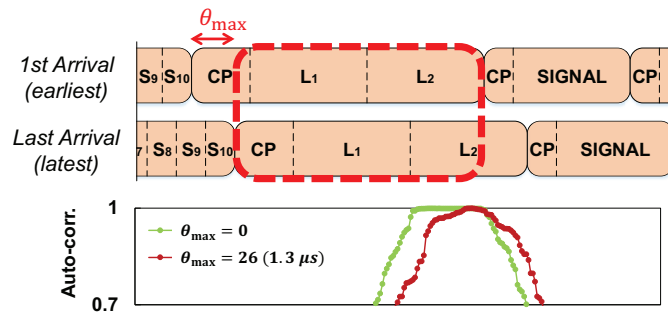
Fig. 10. Combined UL MU signal in the worst scenario of $\theta_{\max} = 1.3$ μs, and corresponding values of $a(n)$ in (13) with $K_a = 64$ & $d = 64$. 3.2 μs-repetition remains over the intersection of L-LTFs, and accordingly the auto-correlation can roughly detect the L-LTF/L-SIG boundary of the earliest UL MU frame.

MU frames, which have been generated as indicated in the preceding Trigger frame.

Note that while this time-domain synchronization is indispensable for acquiring the first boundaries of HE-STF[4] and HE-LTFs as a reference, its accuracy affects the performance of fine calibration where individual STOs are estimated using the provisional HE-LTFs.

2) Fine calibration: With reference to the symbol timing obtained in time-domain synchronization, we move on to HE-LTFs supposed to begin at $\hat{n}_{\mathrm{HELTF}}(= \hat{n}_{\mathrm{LSIG}} + 2N_{\mathrm{LSIG}} + N_{\mathrm{HESIGA}} + N_{\mathrm{HESTF}})$, where N_{LSIG}, N_{HESIGA}, and N_{HESTF}, respectively, represent the numbers of time samples in the subscripted fields including CP. From DFT outputs of the provisional HE-LTFs, we can construct the estimated channel matrix $\tilde{\mathbf{H}}(\mathbf{k})$ for all the subcarrier indexes, with its elements $\{\tilde{\mathbf{H}}(\mathbf{k})\}_{ju} = \tilde{H}_j^u(k)$. While these channel gains may have been corrupted by STO induced from time-domain synchronization error, we utilize them to estimate the individual STOs of concurrent frames as each per-STA channel gain $\tilde{H}_j^u(k)$ holds linear phase offset inherently.

Now the individual STO, $\tilde{\delta}_u$, for UL MU frame from the u-th STA can be estimated by

$$\tilde{\delta}_u = \max_j \left[\left| \frac{N_{\mathrm{DFT}}}{2p\pi} \cdot \angle \left\{ \sum_{\{k,k+p\}\subset \mathrm{K}_u} \{\tilde{H}_j^u(k)\}^* \cdot \tilde{H}_j^u(k+p) \right\} \right| \right],$$
(23)

using the following relation[5]:

$$\{\tilde{H}_j^u(k)\}^* \cdot \tilde{H}_j^u(k+p)$$
$$\approx \{H_j^u(k)e^{j2\pi k\delta_u/N_{\mathrm{DFT}}}\}^* \cdot \{H_j^u(k+p)e^{j2\pi(k+p)\delta_u/N_{\mathrm{DFT}}}\}$$
$$\approx e^{j2\pi p\delta_u/N_{\mathrm{DFT}}} \cdot |H_j^u(k)|^2,$$

---

[4]HE-STF, consisting of 5 repetitions of 3.2 μs short training symbol, is essential to carry out AGC for multiple streams.

[5]While the accuracy of approximation used for this formula can be dependent on the frequency selectivity of channel, the maximum subcarrier spacing between two adjacent channel coefficients equals 156.2 kHz when $p = 2$ in HE-LTFs, which is well covered by coherence bandwidth of the channel normally considered in wireless mobile environments.

where K_u denotes a set of subcarrier indexes, which are contained in the RU assigned for the u-th STA, i.e., $\mathrm{K}_u \triangleq \{k | k \in [0, N_{\mathrm{DFT}} - 1], \text{ and } u \in \mathrm{U}_k\}$, and p is the smallest index difference between two adjacent subcarriers on which HE-LTF sequence is modulated. From the individual estimated STOs, we can calibrate the symbol timing of HE-LTFs:

$$\hat{n}_{\mathrm{HELTF,calib}} = \hat{n}_{\mathrm{HELTF}} - \max_{u \in \mathrm{U}} \{\tilde{\delta}_u\},$$
(24)

which shifts to the sample index where HE LTFs of the earliest UL MU frame have started. Then using the new HE-LTFs obtained with reference to the calibrated symbol timing, $\hat{n}_{\mathrm{HELTF},calib}$, channel matrices are reconstructed and passed to MMSE/ZF receive module for decoding the subsequent data fields.

Intuitively, the accuracy of STO estimation depends on the number of per-STA channel gains, $\tilde{H}_j^u(k)$, that can be exploited for calculating (23), while the number itself is decided by the size of RU and the number of RX chains at AP. For example, for OFDMA+MU-MIMO scenario in Section IV-A (106-tone RU and four RX chains), if 6.4 μs HE-LTF is used which modulates every other subcarrier with $p = 2$, the total number of available $\tilde{H}_j^u(k)$'s is up to 212 for each frame. Whereas for OFDMA alone scenario (26-tone RU and single RX chain) using the same half symbol HE-LTF, we can exploit only 13 samples of $\tilde{H}_j^u(k)$ to estimate each STO, thus leading to some residual offset from the target symbol timing $\delta^* = 0$. Interestingly, we have observed that the resulting estimation errors are biased toward the positive values of δ^*, and mostly below just 100 ns even at quite low SNRs. Therefore, we recommend that when trying the fine calibration with insufficient amount of channel gains, it should be considered to coerce some pre-offset for compensating the estimation errors as the following (assuming 20 MHz sampling rate):

$$\hat{n}_{\mathrm{HELTF,calib}} = \hat{n}_{\mathrm{HELTF}} - \max_{u \in \mathrm{U}} \{\tilde{\delta}_u + 1\}.$$
(25)

Another point is that the arrival timings of concurrent frames depend on RTDs and LO clock at STAs, both of which are thought to be quasi-static factors in practice. If AP builds a database for recording the differences of estimated STOs between any two STAs in a UL MU, it can be employed as *a priori* information when choosing STAs to join the next UL MU. Specifically, grouping those with small deviations one another will facilitate the use of shorter CP, which yields higher data rate by reducing the transmission overhead.

V. PERFORMANCE EVALUATION

In this section, we evaluate the performance of our proposed symbol timing synchronization methods via extensive link-level simulations. We have implemented both of the proposed time-domain synchronization and fine calibration in our 802.11ax link-level simulator, where all the environmental conditions are configurable. We have also implemented those three state-of-the-art algorithms proposed in [22–24], which addressed CSD issues in MIMO transmissions, to demonstrate the degradation of conventional methods when applied to
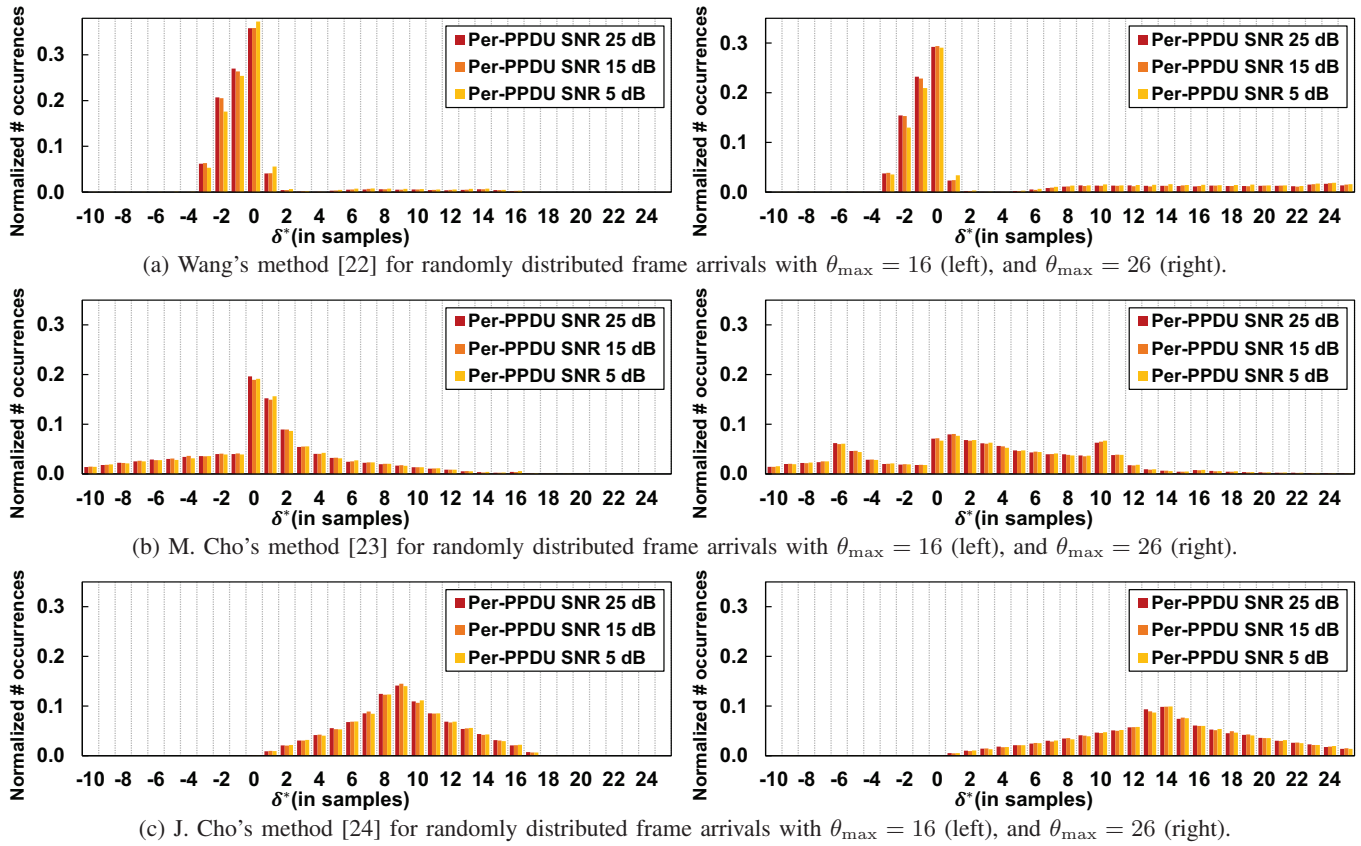
Fig. 11. Performance of the state-of-the-art synchronization algorithms in literature when applied to 9-user UL MU in 20 MHz, where each UL MU frame has an independent random arrival timing following uniform distribution with $\theta_{max} = 16$ ($0.8\ \mu s$) and 26 ($1.3\ \mu s$), assuming TGn "D" NLOS channel ($L = 9$) and that frequency and power pre-correction are ideally performed at participating STAs.

(a) Wang's method [22] for randomly distributed frame arrivals with $\theta_{max} = 16$ (left), and $\theta_{max} = 26$ (right).

(b) M. Cho's method [23] for randomly distributed frame arrivals with $\theta_{max} = 16$ (left), and $\theta_{max} = 26$ (right).

(c) J. Cho's method [24] for randomly distributed frame arrivals with $\theta_{max} = 16$ (left), and $\theta_{max} = 26$ (right).
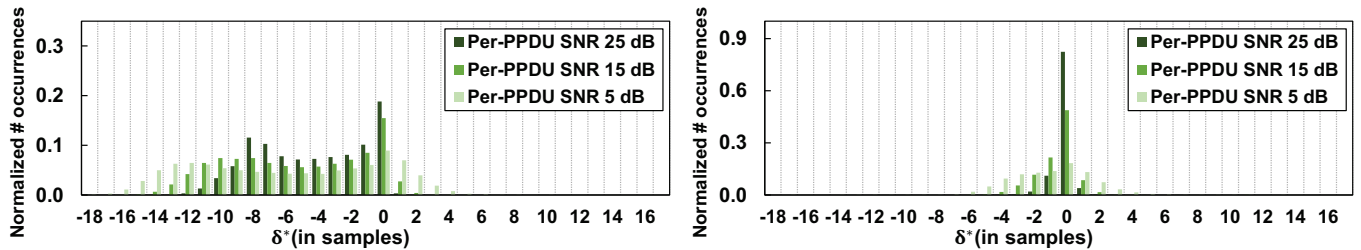

Fig. 12. Performance of the proposed time-domain synchronization in time domain applied to 9-user UL MU, where frame arrival timings are randomly distributed with $\theta_{max} = 16$ (left), and $\theta_{max} = 26$ (right), assuming TGn "D" NLOS channel ($L = 9$) and that frequency and power pre-correction are ideally performed at participating STAs.

802.11ax AP's UL MU receiver and compare them with our proposed methods.

We assume that the arrival timing of each frame in a UL MU follows the uniform random distribution with specific θ_{max} values, not exceeding 1.3 μs in time which is supposed to be the worst-case deviation among STAs. In succession to the previous section, those two representative UL MU scenarios in 20 MHz—OFDMA alone and OFDMA+MU-MIMO—are considered only, but without loss of generality the results can be applied to any UL MU scenarios including wider bandwidth operation which enables to accommodate more STAs in a UL MU. Overall simulation settings are as in Table 1 unless noted otherwise. Lastly, for every simulation run, synchronization modules always begin running at some random instant between the third and sixth legacy short training symbol of the latest

UL MU frame, taking into account the unpredictable AGC settlement delay [17].

To verify both the precision of our methods and the practical benefits attainable in UL MU by adopting them, the simulation results are presented focusing on largely two different perspectives: Synchronization accuracy and data delivery via UL MU.

A. Synchronization Accuracy

Performance of the techniques in literature: We firstly present the performance of the state-of-the-art algorithms when applied to receiving UL MU, which have been originally designed for SU on legacy 802.11 receivers. As for implementation, the window parameters for calculating the key metrics
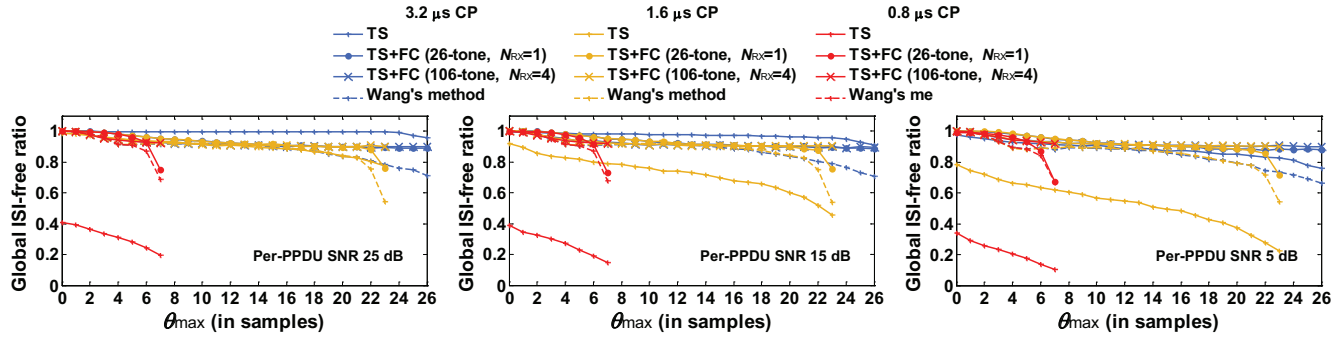
Fig. 13. Global ISI-free ratio versus $\theta_{\max}$ for three different CP lengths. Time-domain synchronization used alone (TS) and in combination with fine calibration (TS+FC) for two different UL MU scenarios are compared with Wang's method proposed in [22].
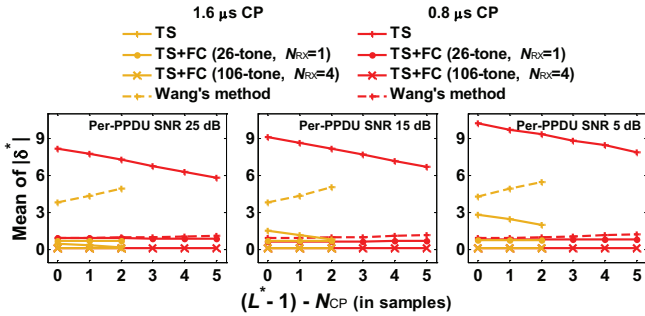

Fig. 14. Mean of $|\delta^*|$ for two different CP sizes when there cannot be global ISI-free region for $L^* - 1 > N_{\mathrm{CP}}$.

in each algorithm are tuned to some suitable values, obtained by exhaustive search for the utmost performance.

Fig. 11 shows the normalized number of occurrences of the resulting STO with respect to the earliest frame, δ^*, running each algorithm to receive UL MU in 20 MHz from 9 STAs, under three different per-PPDU SNR levels[6], namely, P_T^u/N_0. While the STO distribution resulting from each algorithm maintains its tendency over different per-PPDU SNR levels, it is widely scattered and biased toward the positive values of δ^* in common. We can infer that the symbol timing found via conventional methods is prone to severe MUDR degradation, from this STO distribution and the MUDR degradation under δ^* in Fig. 9. Among those three state-of-the-art algorithms, as shown in Fig. 11(a), Wang's method performs the best managing to provide the high probability of δ^* within the global ISI-free region, by virtue of utilizing the SIR-based metric which could neutralize the effect of multiple cross-correlation peaks.

Behavior of the proposed time-domain synchronization: We now demonstrate the operation of our time-domain synchronization method, in the same scenario where AP receives concurrent frames from 9 STAs. Fig. 12 shows the normalized number of occurrences of δ^* for the symbol timing determined by (22). Unlike the results by other state-of-the-art methods in Fig. 11, our time-domain synchronization does not yield

STO distribution biased toward the positive values even under $\theta_{\max} = 26$ as shown in the right part of Fig. 12. It rather converges to around the desired symbol timing of $\delta^* = 0$ under larger $\theta_{\max}$, as the intersection of L-LTFs gets smaller and makes sharper auto-correlation peak, as depicted by the red dots in Fig. 10.

On the other hand, the STO distribution spreads toward the negative values under small $\theta_{\max}$ as shown in the left part of Fig. 12. This is because of the auto-correlation plateau along the intersection of L-LTFs, as depicted by green dots in Fig. 10. As will be verified later, the biased STOs under small deviation of arrival timings are quite tolerable, since the small $\theta_{\max}$ allows the wide range of global ISI-free region on $\delta^* < 0$ at the same time. For this reason, while the behavior of our time-domain synchronization method is exactly the opposite of Wang's method shown in Fig. 11(a), it is better suited to UL MU covering more extensive cases of arrival timings.

Global ISI-free region: Next, we evaluate the precision of the proposed methods, i.e., time-domain synchronization used alone (TS) and time-domain synchronization in combination with fine calibration (TS+FC), in comparison with Wang's method [22] which has performed the best among those three state-of-the-art methods in Fig. 11. As noted earlier, the performance of our fine calibration depends on the number of per-STA channel gains that can be exploited for STO estimation in the frequency domain. Accordingly, TS+FC is evaluated separately for each of those two UL MU scenarios, i.e., OFDMA alone and OFDMA+MU-MIMO, which correspond to TS+FC (26-tone RU, $N_{\mathrm{RX}} = 1$) and TS+FC (106-tone, $N_{\mathrm{RX}} = 4$), respectively. Fig. 13 presents the performance of each scheme in terms of "global ISI-free ratio" defined as the ratio of resulting δ^* within the global ISI-free region given by (17), for different CP sizes and per-PPDU SNR levels. Note that each curve is plotted on the specific range of $\theta_{\max}$, where the global ISI-free region exists for the corresponding CP size.

In Fig. 13, TS+FC shows the highest global ISI-free ratio over Wang's method, under all possible values of $\theta_{\max}$ and CP sizes. Especially when employed with sufficient number of per-STA channel gains in OFDMA+MU-MIMO scenario (106-tone, $N_{\mathrm{RX}} = 4$), it always achieves over 90% of global ISI-free ratio regardless of the circumstances. Besides, we observe that our fine calibration is highly robust to low-SNR

---

[6] Per-PPDU SNR is defined as the ratio of time-domain received signal strength measured at legacy PLCP preamble of each UL MU frame to the receiver's noise level.
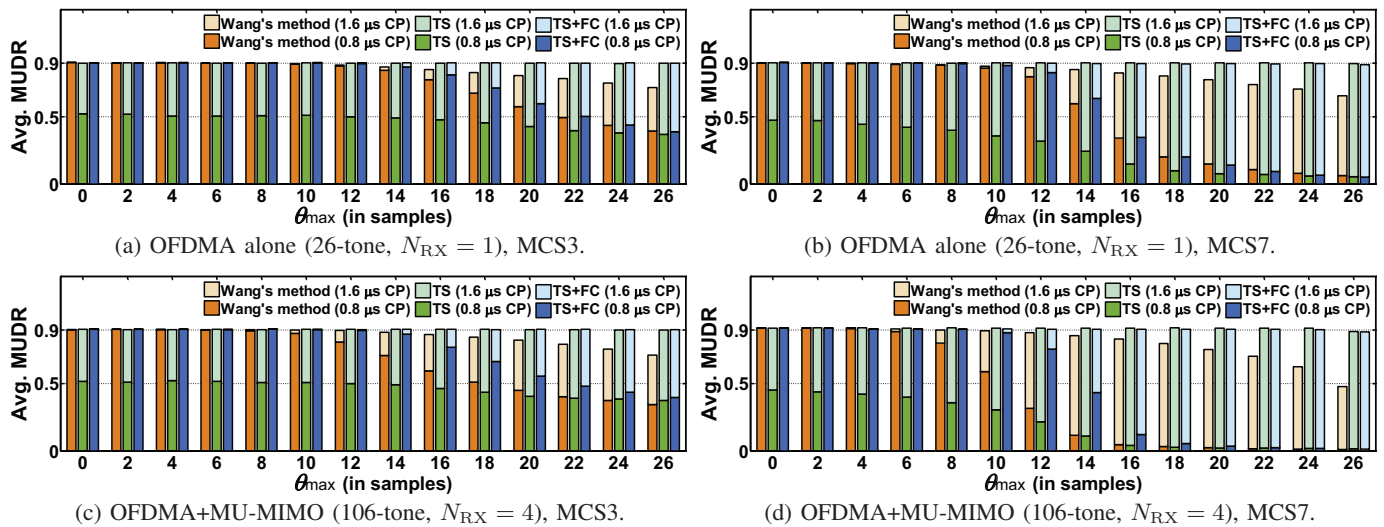
This article has been accepted for publication in a future issue of this journal, but has not been fully edited. Content may change prior to final publication. Citation information: DOI 10.1109/ACCESS.2018.2881980, IEEE Access

13

Fig. 15. Average MUDR versus $\theta_{\max}$, with SNR set to fixed levels where perfectly synchronous UL MU achieves $\sim$90% MUDR. Time-domain synchronization used alone (TS) and in combination with fine calibration (TS+FC) are compared with Wang's method [22], for each case of using two short CPs, 0.8 μs CP (16 samples in 20 MHz) and 1.6 μs CP (32 samples in 20 MHz).

environments and is also resilient to STOs induced from time-domain synchronization step, while the performance of TS is notably deteriorated in lower SNR. Meanwhile, although Wang's method also shows robustness to low SNR owing to its SIR-based metric that is calculated via cross-correlation results, it cannot cover large $\theta_{\max}$ scenarios thereby getting scattered toward the positive δ^* as demonstrated earlier.

Without global ISI-free region: We turn to the situation where the global ISI-free region does not exist for $L^* - 1 > N_{\text{CP}}$, by extending $\theta_{\max}$ to some larger values from the previous simulation settings except the largest CP size. Instead of the global ISI-free ratio, we calculate the mean of $|\delta^*|$ resulting from each synchronization scheme under different SNR levels. The result in Fig. 14 indicates that TS+FC well finds the symbol timing of the earliest frame, thus making the mean of $|\delta^*|$ close to zero, which provides the best MUDR on average as described in Section IV-A. Specifically, it achieves the mean of $|\delta^*|$ below 1 and 0.2 in 20 MHz time samples, for TS+FC (26-tone RU, $N_{\text{RX}} = 1$) and TS+FC (106-tone, $N_{\text{RX}} = 4$) respectively. On the other hand, consistent with the results of global ISI-free ratio, Wang's method fails to find the symbol timing close to $\delta^* = 0$ under large $\theta_{\max}$, and yields large deviation shown in the results of 1.6 μs CP in Fig. 14.

B. Data Delivery

Maximum arrival deviation ($\theta_{\max}$) and CP size (N_{CP}): Now we verify the practical advantage of adopting our proposed methods in terms of data delivery via UL MU. Again, MUDR defined in Section IV-A is used as the evaluation metric. With the SNR set to some fixed levels where $\sim$90% MUDR is achievable for perfectly synchronous UL MU, we have evaluated MUDR under different maximum arrival deviation ($\theta_{\max}$) and two short sizes of CP, i.e., 0.8 μs and 1.6 μs. Fig. 15 shows the average MUDR performance with MCS3 and MCS7, for the two UL MU scenarios. The height of lower

bars indicates the average MUDR for using the shortest 0.8 μs CP (16 samples in 20 MHz), and the height of stacked bar represents the average MUDR for using the medium 1.6 μs CP (32 samples in 20 MHz).

Employing either of our proposed methods with the medium size CP, there seems little MUDR degradation even under the largest $\theta_{\max}$ although the global ISI-free region does not exist. This is because our proposed methods well capture δ^* adjacent to zero, at which AP's UL MU receiver is quite resilient as validated in Section IV-A. Especially note that TS achieves comparable MUDR with TS+FC, while it yields poor global ISI-free ratio as well as scattered STO distribution under small $\theta_{\max}$ shown in Section V-A. STO induced from time-domain synchronization mostly resides in the vicinity of global ISI-free region with the 32-sample CP, and thus causes no serious harm on decoding performance. On the other hand, MUDR is severely aggravated under large $\theta_{\max}$ when employing Wang's method, since its STO distribution gets spread toward the positive values.

For using the shortest 16-sample CP, TS shows poor performance due to its scattered STO distribution much broader than the global ISI-free region. TS+FC and Wang's method provide stable MUDR around $\sim$90% under small maximum deviation, but their performances are also degraded when $\theta_{\max}$ increases. As the arrival timing deviation gets too large to be covered with the shortest CP, capturing the symbol timing of the earliest frame even causes severe interference among STAs, thus not guaranteeing desired decoding performance any more. In this situation, we shall just discard the use of the shortest CP. Meanwhile, TS+FC is still more resilient than Wang's method showing gradual degradation, since it tries to capture the exact symbol timing of $\delta^* = 0$ with higher precision regardless of $\theta_{\max}$.

Overall, the performance of data delivery is more affected by symbol timing synchronization and induced interference when using high MCS and multiple spatial streams. Therefore,

we can infer from these results in Fig. 15 that whether AP should enable the use of the shortest or the medium size of CP in triggering UL MU depends on environmental factors, i.e., maximum arrival deviation (θ_{max}) and channel delay spread (L), as well as transmission parameters including MCS, number of spatial streams used for UL MU, and so on. For example, when receiving UL MU with TS+FC in the same scenario as in Fig. 15(d), we can expect almost ideal performance using the shortest CP, only under θ_{max} below 0.5 μs. For larger θ_{max}, however, we shall use the 1.6 μs CP not to be affected by mutual interference among concurrent frames.

VI. Conclusion

We have shown that the conventional 802.11 symbol timing synchronization methods fail to find a proper symbol timing when receiving asynchronously arriving UL MU, thus causing ISI and ICI which lead to severe degradation of decoding performance. Analyzing the effect of symbol timing misalignment on UL MU decoding performance, we have proposed a novel symbol timing synchronization method exploiting both legacy 802.11 preamble and extended HE preamble. By synchronizing on the proper symbol timing, the proposed method has not only improved UL MU decoding performance but also enhanced efficiency by promoting the use of shorter CP. As high efficiency and UL MU are the goal and the key features of 802.11ax, respectively, this work is expected to highly contribute to the successful introduction of 802.11ax.

Acknowledgment

References

[1] "Global mobile data traffic forecast update, 2016-2021," Cisco VNI, White Paper, Mar. 2017.
[2] IEEE 802.11n-2009, *Part 11: Wireless LAN Medium Access Control (MAC) and Physical Layer (PHY) specifications*, IEEE std., Mar. 2012.
[3] IEEE 802.11ac-2013, *Part 11: Wireless LAN Medium Access (MAC) and Physical Layer (PHY) specifications. Amendment 4: Enhancements for Very High Throughput for Operation in Bands below 6 GHz*, IEEE std., Dec. 2013.
[4] L. Wei and C. Schlegel, "Synchronization requirements for multi-user OFDM on satellite mobile and two-path Rayleigh-fading channels," *IEEE Trans. Commun.*, vol. 43, no. 234, pp. 887–895, 1995.
[5] M. Morelli, C.-C. J. Kuo, and M-O. Pun, "Synchronization techniques for orthogonal frequency division multiple access (OFDMA): a tutorial review," *Proceedings of the IEEE*, vol. 95, no. 7, pp. 1394–1427, 2007.
[6] M. Park *et al.*, "Effects of asynchronous MAI on average SEP performance of OFDMA uplink systems over frequency-selective Rayleigh fading channels," *IEEE Trans. Commun.*, vol. 58, no. 2, pp. 586–599, 2010.
[7] H. Sari, G. Karam, and I. Jeanclaude, "Transmission techniques for digital terrestrial TV broadcasting," *IEEE Commun. Mag.*, vol. 33, no. 2, pp. 100–109, 1995.
[8] S. Kaiser and W. A. Krzymien, "Performance effects of the uplink asynchronism in a spread spectrum multi-carrier multiple access system," *Eur. Trans. Telecommun.*, vol. 10, no. 4, pp. 399–406, 1999.
[9] M. Morelli, "Timing and frequency synchronization for the uplink of an OFDMA system," *IEEE Trans. Commun.*, vol. 52, no. 2, pp. 296–306, 2004.
[10] H. Zeng, H. Li, and Q. Yan, "Uplink MU-MIMO in asynchronous wireless LANs," in *Proc. of the 18th ACM International Symposium on Mobile Ad Hoc Networking and Computing*, 2018.
[11] IT++. [Online]. Available: http://itpp.sourceforge.net/.
[12] M. Speth, S. Fechtel, G. Fock, and H. Meyr, "Optimum receiver design for wireless broadband systems using OFDM, Part I," *IEEE Trans. Commun.*, vol. 47, no. 11, pp. 1668–1677, 1999.
[13] H. A. Mahmoud and H. Arslan, "Error vector magnitude to SNR conversion for nondata-aided receivers," *IEEE Trans. Wireless Commun.*, vol. 8, no. 5, pp. 2694–2704, 2009.
[14] V. E. *et al.*, *TGn channel models*, IEEE 802.11-03/940r2, Jan. 2004.
[15] T. M. Schmidl and D. C. Cox, "Robust frequency and timing synchronization for OFDM," *IEEE Trans. Commun.*, vol. 45, no. 12, pp. 1613–1621, 1997.
[16] A. J. Coulson, "Maximum likelihood synchronization for OFDM using a pilot symbol: algorithms," *IEEE J. Sel. Areas Commun.*, vol. 19, no. 12, pp. 2495–2503, 2001.
[17] A. Fort and W. Eberle, "Synchronization and AGC proposal for IEEE 802.11a burst OFDM systems," in *Proc. IEEE GLOBECOM*, 2003.
[18] S. Chang and B. Kelley, "Time synchronisation for OFDM-based WLAN systems," *Electronics Letters*, vol. 39, no. 13, pp. 1024–1026, 2003.
[19] A. Troya *et al.*, "Efficient inner receiver design for OFDM-based WLAN systems: algorithm and architecture," *IEEE Trans. Wireless Commun.*, vol. 6, no. 4, pp. 1374–1385, 2007.
[20] Y-C. Wu *et al.*, "Maximum-likelihood symbol synchronization for IEEE 802.11a WLANs in unknown frequency-selective fading channels," *IEEE Trans. Wireless Commun.*, vol. 4, no. 6, pp. 2751–2763, 2005.
[21] M. J. Canet *et al.*, "FPGA implementation of an OFDM-based WLAN receiver," *Microprocessors and Microsystems*, vol. 36, no. 3, pp. 232–244, 2012.
[22] D. Wang and J. Zhang, "Timing synchronization for MIMO-OFDM WLAN systems," in *Proc. IEEE Wireless Communications and Networking Conf.*, 2007.
[23] M. Cho, Y. Jung and J. Kim, "Symbol timing synchronization for IEEE 802.11n WLAN systems," in *First Asian Himalayas Conference on Internet*, 2009.
[24] J. Cho, H. T. Anh, J. Kim, and W-K. Cho, "Architecture of timing synchronization for MIMO-OFDM WLAN systems," in *Proc. of the 4th IEEE International Conference on Circuits and Systems for Communications*, 2008.
[25] IEEE 802.11ax-2017, *IEEE Proposed TGax draft specification, IEEE P802.11ax/D2.0*, IEEE Std., Oct. 2017.
[26] S. Yoo *et al.*, "Toward realistic WiFi simulation with smartphone "Physics"," in *Proc. IEEE WoWMoM*, Sydney, Australia, Jun. 2014.